Mechanism and Control of a One-Actuator Mobile Robot Incorporating a Torque Limiter

Satoshi Ito[1] · Shoya Sugiura[2] · Yuya Masuda[1] · Shumpei Nohara[1] · Ryosuke Morita[1]

Abstract

This study presents a novel mechanism for the control of a wheeled robot maneuvering with a single actuator. Elements of snakeboard and two-wheeled skateboard propulsion are applied to the design. Two passive wheels, i.e., casters whose orientation can be controlled, are attached in the back and front of the robot body, and a rotor rotates above the body to induce body propulsion using its counter torque. Three degrees of freedom of motion, i.e., the orientation of the rotor and each of the two casters, are mechanically coupled to the single actuator via a torque limiter. The stoppers are set to restrict the angle of the caster orientation, and a torque limiter allows the rotor to continue rotating without being affected by the stopper's restriction to the range of motion. Experiments demonstrate that the sinusoidal rotor rotation can propel this robot forward and that adding the increasing or decreasing offset to the sinusoidal rotor rotation can curve the robot's motion. Next, a method to position the robot at a specified goal position is proposed, assuming that the current position of the robot is detectable in every control cycle. This method adjusts the rate of increase or decrease of the offset in sinusoidal rotor rotation depending on the direction of the goal position. Introducing the motion capture system enables the robot to successfully reach the specified goal positions.

1 Introduction

Mobility enables robots and animals to not only utilize spatially distributed resources or services but to also deliver resources or services. This mobility is currently realized based on two mechanisms. One is a wheeled mechanism, found in many mechanical systems, where numerous disks that contact the ground are driven to accelerate the main body. The other is a falling-forward motion found in human locomotion, where the instability resulting from gravitational force is the essence of the progression [1, 2]. However, a third mechanism has been studied, which is free from wheel driving and tumbling. This third type of mobile system always maintains static balance and only utilizes passive wheels. This mechanism is found in snake-type robots, roller racers, snakeboards, inline-skates, and other systems. Hirose [3] identified three basic configurations of mobile robots, where these passive wheel systems are considered to be a Wheel-Actuated Body, or belong to the Wheel-Leg, in his classification.

Because all of them possess passive wheels, the driving force that propels a wheeled system must be generated using degrees of freedom (DoFs) of motion other than the wheels. Owing to this, it is advantageous, from a manufacturing cost or maintenance perspective, for such a propulsion system to be realized using only a single actuator. On the basis of this idea, this paper attempts to achieve this passive-wheel driving mechanism under the constraint of using only a single motor.

Actually, snake-type robots [4–6] are typically passive wheeled systems comprising many body segments with two passive wheels on the side connected by the active joints. However, this type of robot typically has more than three body segments, and thus, multiple motors are required. The roller racer[7, 8] can be regarded as a two-segment snake-type robot as it achieves propulsion using a single actuator.

✉ Satoshi Ito
satoshi@gifu-u.ac.jp

1 Faculty of Engineering, Gifu University, Gifu, Japan

2 Graduate School of Natural Science and Technology, Gifu University, Gifu, Japan

However, this propulsion mechanism seems to depend on the powerful drive of the steering located at a single joint, and thus it lacks long gliding achieved by the rolling of the passive wheels, based on our riding experiences.

Compared with the roller racer, human-steered inline-skates and skateboards exhibit faster running or quicker turning. Usually, a human begins skating or boarding by kicking the ground to obtain the required initial acceleration. However, these passive-wheel systems can only be propelled using a coordinated movement of the human operator's entire body while keeping the foot positions fixed with respect to the base of the passive-wheel system, i.e., without kicking the ground. Considering that such a high degree of maneuverability is produced by trained human motion, a robotic system mimicking skating or skateboarding would be expected to require multiple actuators. In fact, some snakeboard robots [9], a type of segmented skateboard, have been designed to use three motors. The snakeboard is extensively studied from the control perspective because of its non-holonomic velocity constraints [10–13].

Inspired by a two-wheeled skateboard, which is capable of rapid movement, though we found later that its propulsion principle is the same as the snakeboard, we attempt to build a skateboard robot with only one motor, rather than traditional designs, which use three motors [9, 14]. Some papers treat this two-wheeled skateboard from a kinematics [15], motion planning [16], or acceleration [17] perspective. However, no projects other than ours [18] appear to be focused on the propulsion of a robot using a single motor based on the behaviors of two-wheeled skateboards or snakeboards.

To achieve single-motor propulsion, particular types of mechanical devices are required. Section 2 of this paper presents a new mechanism combining a torque limiter with stoppers and demonstrates propulsion using the robot constructed by us. In Section 3, we describe the experiments of straight and curved motion, which we conducted based on sinusoidal rotor motions, and experimentally discuss the best combination of amplitude and frequency for sinusoidal motion. Section 4 examines leading the robot to a specified goal position using positional feedback, and finally, Section 6 concludes this paper.

2 One-actuator Driving Mechanism

2.1 Two-wheeled Skateboard

The wheeled system proposed herein treats a two-wheeled skateboard as a reference model.

The two-wheeled skateboard comprises two plates under which an eccentric curving caster is attached, with its curving axis reclined backward. The plates are connected front to back by one axis with a torsion spring. Owing to the placement of the torsion spring, the two plates normally form a flat surface where skateboard riders can place their feet. In such a case, at that instance, the caster faces ahead, as shown in the top photo of Fig. 1a, and the skateboard travels straight. However, when the riders shift their weight to either side from above this longitudinal axis, the two plates twist with respect to each other. This changes the orientation of the casters under the plate owing to the backward reclined orientation of the caster to the plate, as shown in the bottom photos of Fig. 1a.

Riders usually obtain initial momentum by kicking the ground using one foot while the other foot remains placed on the skateboard. However, riders are also able to propel the skateboard through their own motion by twisting their upper body around the waist, thereby controlling the wheel direction, as shown in Fig. 1b.

Using this approach, the following three motions are simultaneously required for human riders to propel such a skateboard:

M1.   a balancing motion to avoid lateral falls;
M2.   a weight shift motion to change or maintain the orientation of the casters; and
M3.   a waist twisting motion to obtain a propulsion force.

Riders repeat motions M2 and M3 by alternating the direction of their motion at appropriate times. With the caster turned to the left, the rider twists their upper body to the right. Next, with the caster turned to the right, the rider conversely twists their upper body to the left and repeats the cycle. Then, the skateboard progresses with laterally undulation.

2.2 Robotic Design

2.2.1 Design Perspective

This study attempts to realize the propulsion observed in two-wheeled skateboard with equipping the single motor only.

To simplify the robot's control mechanism, the lateral balance control (M1) was disregarded and attention was concentrated only on the essence of the skateboard's propulsion. This can be achieved by using side support wheels in the robot.

Next, the board was designed, not as two plates connected by the torsion spring, but as a simple single plate, which can remove one DoF associated with the roll

Fig. 1 A two-wheeled
skateboard
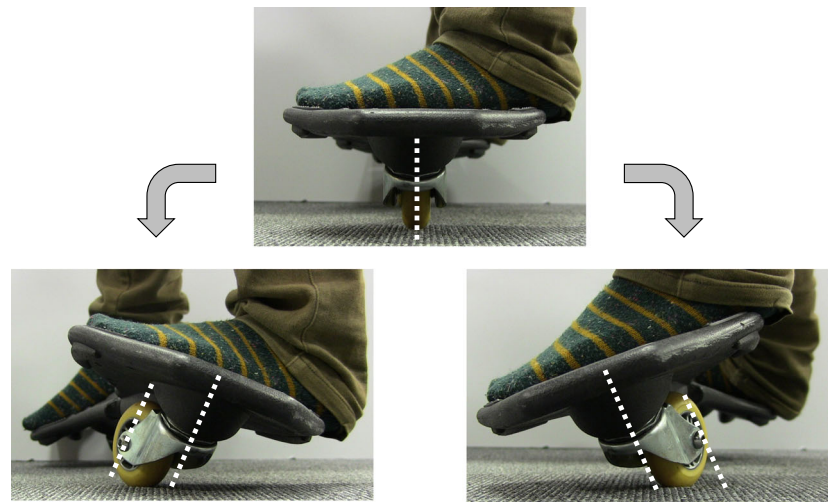
(a) Changes in wheel orientation by the twisting of the skateboard.

Rotation of waist

Lateral balance of the body

Torsion of board
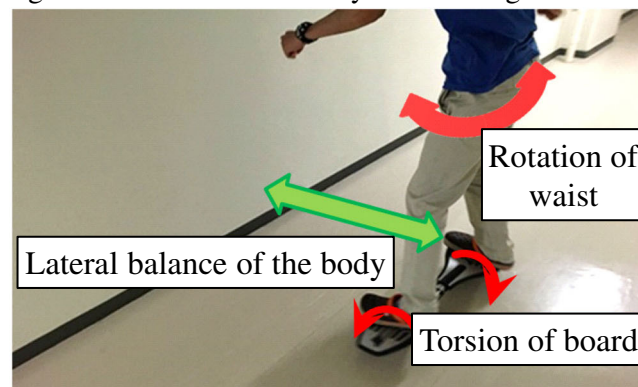
(b) Rider movement on the skateboard.

direction. Indeed, this two-plate structure was needed to produce the change of the caster orientation by the human M2 motion. However, we will replace this function by a direct-drive caster orientation. In addition, regarding the wheel orientation, the chosen type of motion, i.e., the deviation of the caster orientation is always symmetrical in the back and forth motion of the casters, was the only one considered. The angles of the caster orientation and its combinations vary from person to person and in each repetition even in the motions performed by the same person. However, results of our study indicate that the symmetrical pattern is one of the possible and promising methods of driving the board.

Finally, principal force driving the board, which is the moment caused by M3, was considered. If the human rides at a slightly deviated position on the board, not only the moment but also the translational force acts on the center of mass (CoM) of the board. Although such a translational force can affect the progression, we only focused on the moment around the CoM in this study to realize the propulsion by referring to the simple method among the feasible ones.

2.2.2 Concept of Propulsion

The essence of the propulsion principle is described as the generation of the counter moment in M3 while maintaining the orientation of the front and rear casters to be symmetrical, i.e., it deviated the same amount in the opposite directions. Similar to the case of the snakeboard model [19], the rotor is introduced at the top of the robot and is rotated to generate the moment. To effectively obtain the moment, the rotation of the rotor is frequently reversed, as is seen by observing riders on a skateboard. In this case, the orientation of the casters should be simultaneously inverted.

To achieve this series of actions, most designs typically require three motors for two casters and one rotor. We will now attempt to reduce the number of required motors to one.

First, the orientation of the two casters will be driven together. Assumption A3 allows us to utilize two gears with the same number of teeth to achieve symmetrical deviation of the caster in the front and rear, driven by a single actuator. Our design is based on the recognition that the caster orientation angle always maintains the same constant magnitude, $+\alpha$ or $-\alpha$.

We then couple the caster and rotor rotations. In this manner, the apparent contradiction of the requirements in the caster and rotor become a serious problem; i.e., the caster must maintain the orientation, including the static requirement, but the rotor should be able to continue the acceleration or deceleration necessary to obtain the moment, i.e., the dynamics requirement. Suppose here that, using a mechanical stopper, the range of motion of a caster orientation is restricted. Then, the maintenance of the caster orientation at $+\alpha$ or $-\alpha$ can be achieved if the caster is rotated until the rotation of the caster reaches the stopper. This simultaneously constrains the rotor rotation if the rotor rotation is directly coupled to the caster rotation.

To avoid this situation, we temporarily disconnect the coupling between the rotor and the caster. We introduce a torque limiter here to implement this decoupling, which cuts the torque transmission if the exerted torque exceeds the designed values.

In summary, we expect the following actions. Within the range of motion of the caster orientation, the motor can rotate both the caster and the rotor, if a torque limiter is selected to drive them within the designed operating limit. When the casters reach the end of their range of motion, a large torque will be exerted owing to the counter force from the stopper. At that point, the torque limiter disconnects the torque transmission, and thus, the rotor can rotate while maintaining the caster orientation angles and generating the propulsion force.

2.2.3 Mechanism Realizing our Concept

Figure 2 shows an experimental implementation of our concept described in the previous section. Figure 2a and b illustrate the movement when the torque limiter is not working. The two disks at the bottom of the figure represent

the front and rear casters, respectively. Their vertical rotation axes are connected to gears B and C, with matching tooth counts, placed in the horizontal main body. The top large horizontal disk represents the rotor, which is directly connected to the sole motor present. The lower part of this motor axis is also connected to gear A via a torque limiter, which can symmetrically and simultaneously change the orientation of the front and rear casters when gear A drives gear B. In this manner, the rotor and orientation of the two casters are simultaneously driven by a single motor.

Next, a stopper mechanism is installed to restrict the range of motion of the caster orientation and maintain a constant angle. When the bar that simultaneously moves the gear and caster hits the stoppers and ceases rotation, the torque limiter begins working, and the casters stop rotating. Thus, the rotor can continue to rotate even if the caster orientation is being maintained, as shown in Fig. 2c.

2.2.4 Robot Construction

Figure 3 shows the robot that we built for our experiments. It is 600 mm in length, 450 mm in width, and 270 mm in height and weighs 3.8 kg. The casters, 40 mm diameter, 38g weight, made by urethane, were attached with 0 mm offset. The wheel base was 190 mm. In a CAD model of this design, we found that the moment of inertia was 0.078 kg $\cdot$m^2 for the robot side, whereas it was 0.053 kg$\cdot$m^2 for the rotor side. Only a single DC motor (Maxon Motor RE25, 20 W, 128:1 reduction ratio) connecting the rotary encoder (Maxon Motor HEDL5540) was installed on this robot. To reduce the height, the upward driving axis directly connected to the motor was folded downward using a couple of equivalent radius gears. Next, a torque limiter (TSUBAKIMOTO CHAIN CO., MK-08) was attached to the driving axis with an attached stopper mechanism. The
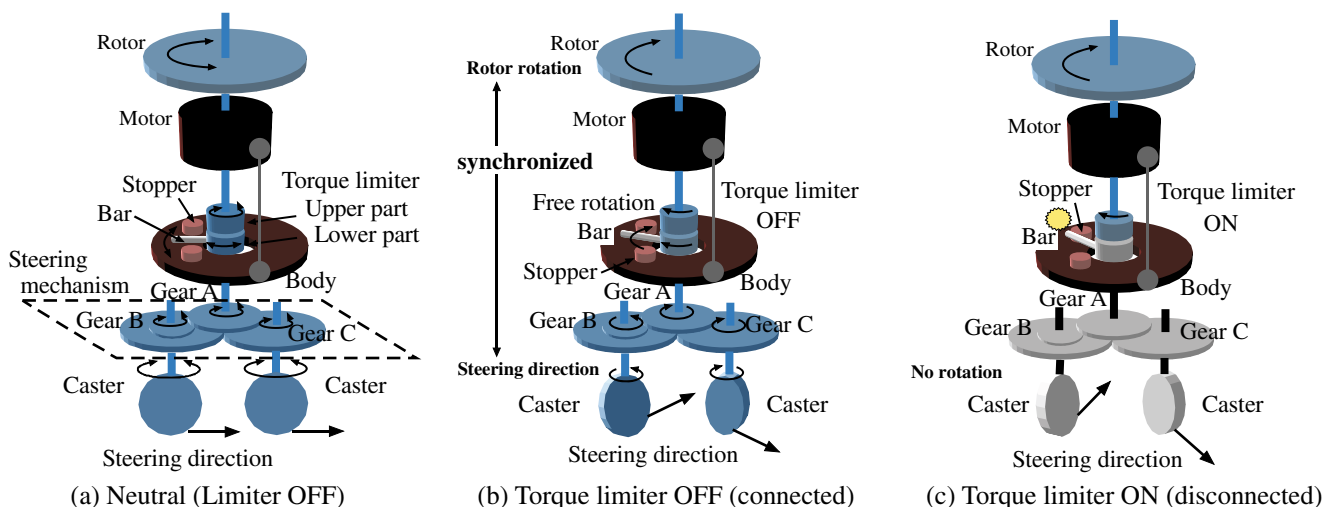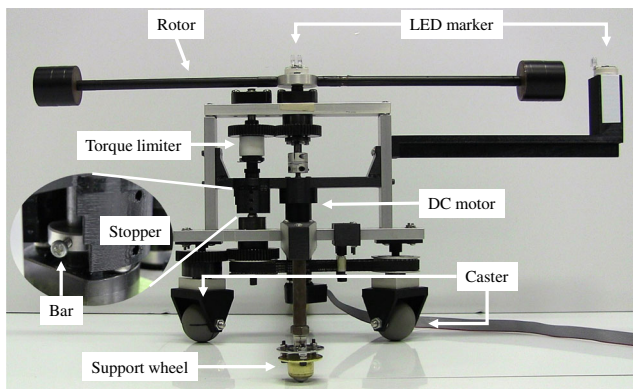

Fig. 2 Movement of the proposed mechanism

Fig. 3 The constructed skateboard robot.

stopper mechanism was designed to mechanically select the caster orientation based on its own positions from 35°, 40°, and 45°. Spherical non-eccentric casters were used to minimize rotational friction with the point contact to the ground. We used omni-directional casters to provide lateral stability and avoid lateral falls.

2.3 Movements

We conducted experiments, which confirmed that the robot does propel itself and does move forward autonomously. In these experiments, the rotor was swung such that its angular deviation tracked a sinusoidal trajectory. The experimental environment is described in Section 3.3.

The photographs of the robot motion, depicted in Fig. 4, show that the robot smoothly accelerated and moved forward with lateral undulations as expected.

3 Experimental Analysis on Straight and Curved Motion

3.1 Purpose

The previous section demonstrated robot propulsion using sinusoidal rotor rotations. However, some other combinations of frequency and amplitude are feasible to achieve sinusoidal rotor motions. Therefore, we attempted to experimentally find the setting that provided the maximum traveling distance for a given amount of time.

Next, although symmetrical rotor rotation with the same clockwise (CW) and counter-clockwise (CCW) deviations is expected to make a robot travel straight, we explored what would happen if the rotation became asymmetrical, where the deviations differed in CW and CCW rotations. We expected that the robot would curve to one side because such rotor rotation would create a difference in the CW and CCW yaw moment that reacts to the main body as the

counter force of the rotor motion. Another experiment was conducted to confirm our expectation.

3.2 Control Input

We set the rotor angle as the object of the control, which is directly connected to the DC motor. We decided to control this using the following PD control:

$$\tau = -K_d \dot{\theta}_R + K_p(\theta_{Rd} - \theta_R), \tag{1}$$

where τ is the motor torque, θ_R and $\dot{\theta}_R$ are the rotor angle deviation and its angular velocity, $\theta_{Rd} = \theta_{Rd}(t)$ is the desired trajectory of the rotor angle, and K_d and K_p are the derivative and proportional gains, respectively.

3.3 Experimental Environment

Figure 5 illustrates the experimental environments constructed in this paper. The PC controller, with a D/A converter board and an encoder counter board, outputs the control signal every 1 ms. This control signal is transferred to the motor driver, which generates a pulse width modulation signal to drive the DC motor of the robot. In reverse, the signals produced by the rotary encoder of the motor are sent to the encoder counter board, which measures the rotation angles.

A 3D motion capture system (Library Co. Ltd., Radish) was used to detect the robot position within the workspace of 230 cm in length by 360 cm in width. This system measured the position of the LED markers attached to the robot and sent them to the PC controller using the UDP communication protocol every 20 ms.

3.4 Straight Movement Experiments

3.4.1 Conditions

The desired trajectory of the rotor angle was set as follows:

$$\theta_{Rd}(t) = A \sin(2\pi f t), \tag{2}$$

where three frequencies, $f = 0.7$, 0.8, and 0.9 Hz, were tested for each amplitude A that was changed every 5°. The caster orientation was set at $\alpha = 35°$, 40°, and 45°.

The traveling distance was evaluated as the straight distance between the start and final robot positions in 8 s experiments. The traveling distance was measured thrice for every experimental configuration.

3.4.2 Results

The experiments began from $A = \alpha + 5$ because it was necessary for the rotor's rotation to be larger than the
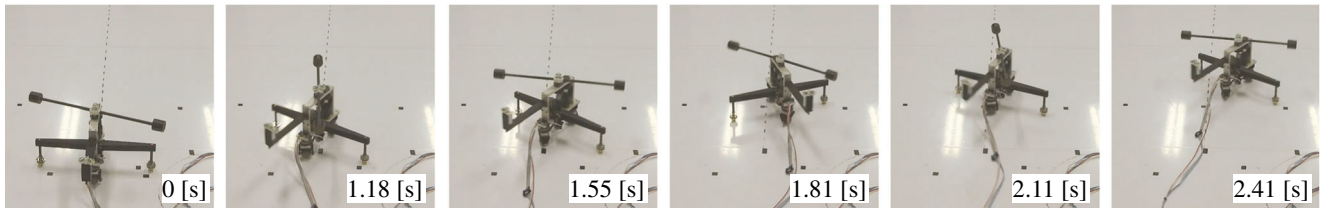
Fig. 4 Propulsion experiment using sinusoidal rotor rotation

changing range of the caster orientation, i.e., $A > \alpha$, for the caster orientation to be completely switched.

The gains were set as $K_d = 0$ and $K_p = 1$. Figure 6 depicts the obtained result.

The maximum traveling distance was 147 cm for $\alpha = 35°$ ($A = 55°$; $f = 0.8$ Hz), 164 cm for $\alpha = 40°$ ($A = 55°$; $f = 0.8$ Hz), and 178 cm for $\alpha = 45°$ ($A = 60°$; $f = 0.8$ Hz). At the unfilled plots in Fig. 6, the casters appear to have slipped, implying that the constraints of the traveling distance evaluation were inconsistent with those of the experiment controls. Hence, these values were removed from the evaluation of the maximum traveling distance.

3.4.3 Remarks

The experiments indicate that the changing range of the caster orientation barely affects the combination of frequency and amplitude that provides the maximum travel distance. However, this maximum distance differs for the frequency and amplitude combinations. Consequently, the changing range of the caster orientation is suitable at 45°.

Observation of the robot experiments indicates that the traveling direction of the robot potentially differs from the direction the robot had initially been facing toward. To investigate this phenomenon, anti-phase desired trajectories were input at the same initial position, and the direction

of the robot was set with the following settings $\alpha = 45°$; $A = 50°$; and $f = 0.8$ Hz. Figure 7 shows the resultant paths of robot movement. The original phase input shifts the path rightward, and the anti-phase input shifts it leftward. This demonstrates that path deviations from the initial robot direction originate from the initial phase of the sinusoidal signal for rotor rotation.

We interpreted this result as follows. The original periodic sinusoidal input causes the robot to curve toward the left at the first half period, and then, curve to the right during the last half period. If this occurs in the steady state, the amount of left and right curving will equalize as the yaw moment that the rotor generates is the same in both half periods owing to the symmetry of the sine wave. This results in overall straight robot motion over multiples of a full phase period. However, at the transient state, this is not the case. With the rotor stopped at the initial state, the amplitude and velocity of rotor motion are smaller at the first swing than that at the reversed second swing; i.e., the counter moment at the first swing becomes smaller than the counter moment at the second swing. Consequently, the robot progresses a bit rightward. Of course, the third swing will be greater than the second one, but some experiments show that this robot reaches the steady state in about the third swing. Accordingly, the effect of the first swing's small scale causes the shift of straight motion from the initial orientation.
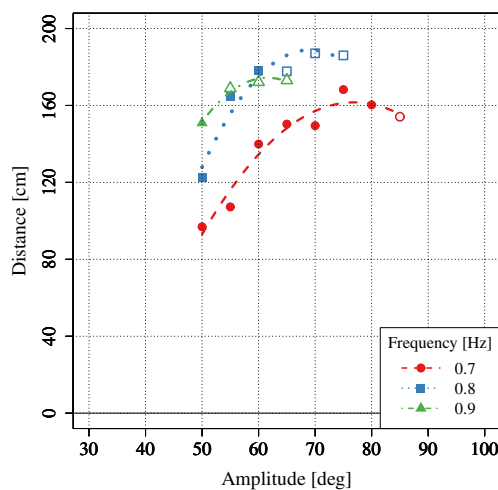
Fig. 5 Control system
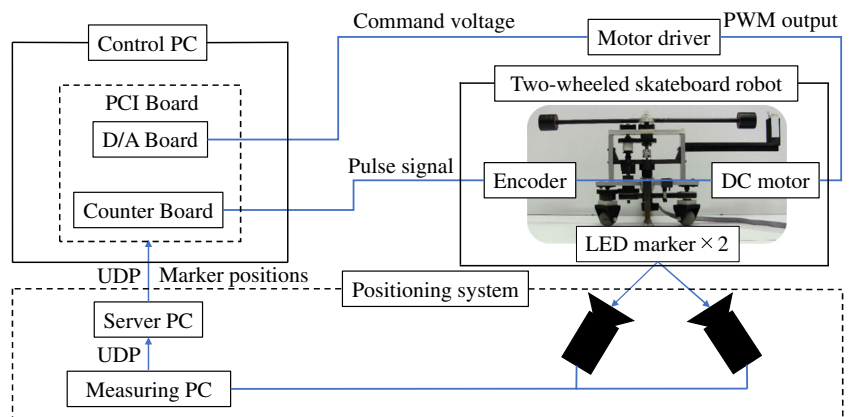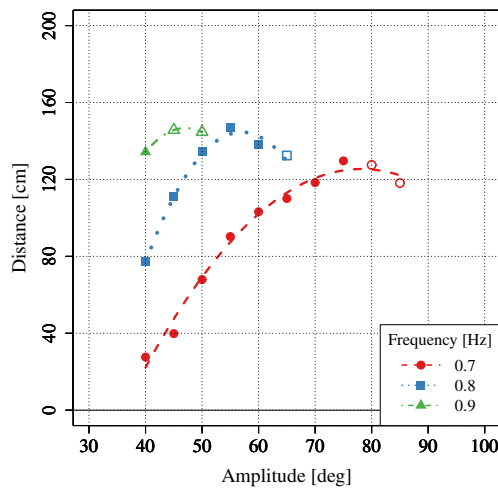
(a) $\alpha = 35°$
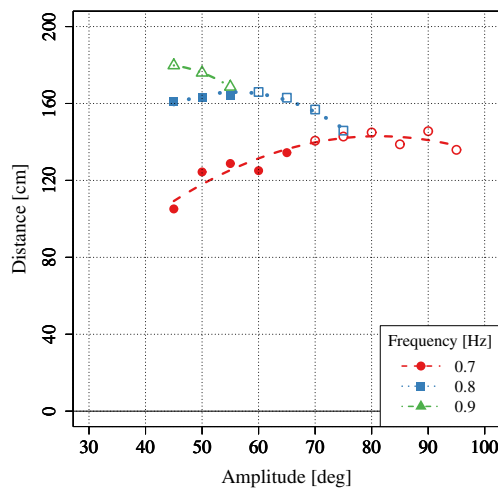
(b) $\alpha = 40°$

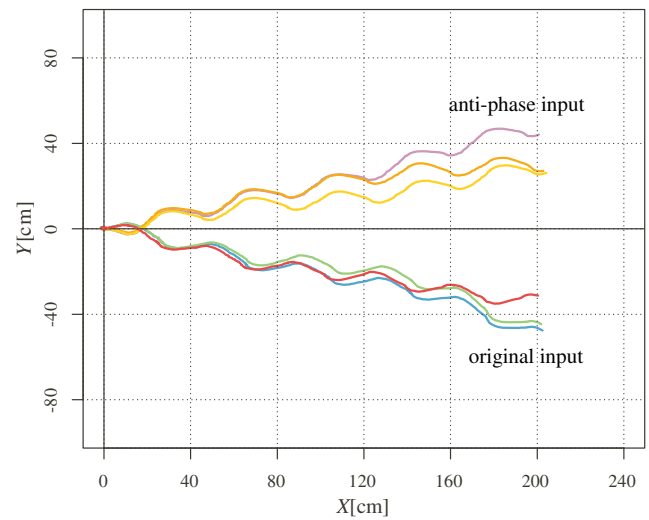(c) $\alpha = 45°$

Fig. 6 Straight motion tests

Fig. 7 Path comparison of straight movements for original and anti-phase inputs

3.5 Curved Movement Experiments

3.5.1 Conditions

Next, the robot movement was experimentally evaluated with respect to asymmetrical rotor rotation to determine whether the robot exhibits the curved motion. The desired trajectory is given as follows:

$$\theta_{Rd} = A \sin(2\pi f t) + \rho \times t \tag{3}$$

Here, ρ denotes the offset rate of change. Based on the results in the previous section, the parameters are set as $A = 50°$ and $f = 0.8$ Hz, considering the avoidance of caster slippage. Then, ρ was increased from 0°/s to 100°/s in 10°/s increments while setting the caster orientation to $\alpha = 35°$, 40°, and 45° for each set of experiments.

The 10 s experiments were conducted thrice for each set of parameters. The first part of each experiment was devoted to straight motion to sufficiently accelerate the robot. Matching the configuration of the straight movement experiments, the gains were set to $K_d = 0$ and $K_p = 1$.

3.5.2 Results

Figure 8 depicts the 10 s paths of the robot. For each set of parameters, only the median path, sandwiched between the other two, was selected for use in these figures. Note here that we have confirmed that the robot can curve to the right with a negative ρ.

(a) $\alpha = 35°$

(b) $\alpha = 40°$

(c) $\alpha = 45°$
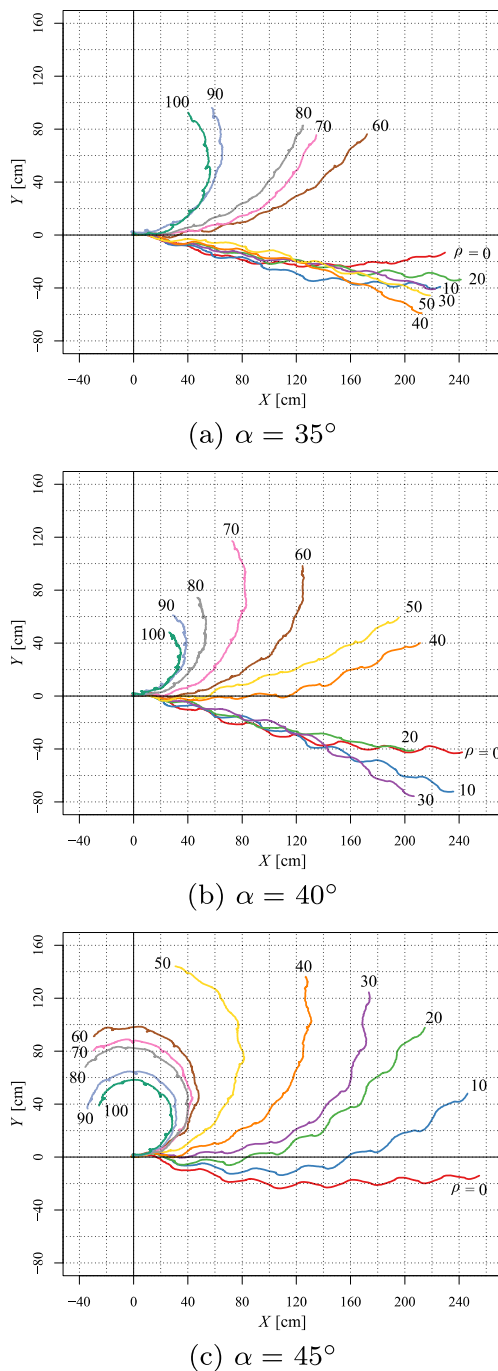
**Fig. 8** Robot paths that change with the offset rate of change

3.5.3 Remarks

The robot showed the expected curved movement when the caster orientation was set to $\alpha = 45°$. However, for the small ρ, the robot seldom curved at $\alpha = 35°$ and $40°$.

Our first idea behind making the robot curve was that the asymmetrical rotor rotation in the CW and CCW directions would create a difference in the counter moment for the main body between the CW and CCW directions. This would result in the difference in traveling distance to the left and right, and thus, the robot will travel toward the larger direction with curving. However, little curved motions were observed in some experiments, e.g., $\rho \leq 50°/s$ in $\alpha = 35°$ or $\rho \leq 30°/s$ in $\alpha = 40°$, which implies that the principle of the actual curved motion could differ from our idea.

One possibility is that the caster orientation did not reach the expected position for the small ρ. Figure 9 shows the course over time of the rotor angle θ_R when ρ is set to $50°/s$ and $60°/s$ for $\alpha = 35°$. As shown in these graphs, the magnitude of the left rotation that causes an increase in θ_R is larger than that of the right rotation because the offset is monotonically increasing. Then, the magnitudes of the right rotation were $70°$ for $\rho = 50°/s$ and $64°$ for $\rho = 60°/s$. Considering that the rotor rotation and curve of the caster orientation are mechanically coupled as 1:1 in the robot, a magnitude of $70°$ completely brings the caster to the limit of its changing range as $70°$ is equal to the movable range of the caster 2α for $\alpha = 35°$. On the contrary, a magnitude of $64°$, which is shorter than 2α, will not reach the limit of the caster rotation, indicating that the right curve is not sharper than the left curve. This is why the robot curved to the left.

Checking the path from this perspective, it could be seen that this explanation is valid at $\alpha = 40°$; i.e., we were able to determine that, unlike our first idea, the reason for the

(a) $\rho = 50°/s$ (b) $\rho = 60°/s$
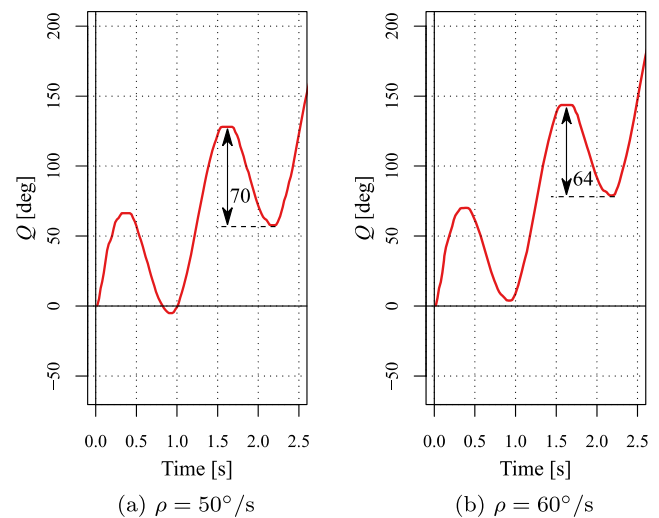
Fig. 9 Rotor rotation angles containing offset increase

curved motion of the robot was the difference between the sharpness of the left and right curved motions, which led to the undulating curved motion.

4 Reaching the Goal Position

4.1 Problem Formulation

Skateboard riders steer a board and finally reach their intended position by continually confirming the direction to a desired goal location. Hence, we question whether it is possible to make a robot autonomously arrive at a specific desired position, similar to how riders use the feedback of current positional information?

This section of the paper challenges the above question and considers a control method for making the robot reach the desired goal position under the following conditions:

C1. The desired goal position $G(x_d, y_d)$ is given at a position sufficiently far from the initial position.
C2. The rotor angle θ_R, robot position (x, y), and its direction angle ϕ_0 are detectable.
C3. The robot is deemed to have arrived at the desired position if the distance to the desired position is less than a value d, set in advance.

4.2 Control Method

A strategy for making the robot turn such that the desired goal position lies ahead of the robot and then travel straight maintaining its direction is used here. The experiment in the previous section demonstrated that the larger is the offset rate of change ρ, the sharper is the curved motion produced and that a zero offset rate of change results in straight movement. Therefore, we interpreted this as indicative that the robot can change its direction such that the goal position is just ahead if the offset rate of change is adjusted based on the relative direction of the goal position to its current position.

Accordingly, the offset rate of change ρ is adjusted on-line by the relative direction θ_G of the goal position

$$\rho = K \times \theta_G, \tag{4}$$

where K is the parameter that determines the speed of the adjustment.

4.3 Detecting the Relative Direction Angle of the Goal Position

The robot position (x, y) and its direction angle ϕ_0 are calculated from the markers' position detected from the motion capture system. One marker is attached to the rotor rotation center, and the other is attached to the rear center line of the main body. The former's position $M_1(x_1, y_1)$ is regarded as the robot's position. On the other hand, the direction of the robot ϕ_0 is defined as the angle between the line connecting two markers and the x-axis of the motion capture system, as illustrated in Fig. 10. Putting the latter's position $M_2(x_2, y_2)$, ϕ_0 can be obtained from

$$\phi_0 = \mathrm{atan2}(y_1 - y_2, x_1 - x_2), \tag{5}$$

where, $\mathrm{atan2}(Y, X)$ returns $\arctan(Y/X)$ within the range $[-\pi, \pi]$ based on the quadrant of point (X, Y). Because the angle ϕ_G between the line from the current robot position to the goal position and the x-axis can be calculated as follows:

$$\phi_G = \mathrm{atan2}(y_d - y_1, x_d - x_1), \tag{6}$$

the relative direction of the goal position, θ_G in (4), is defined as the difference between ϕ_G and ϕ_0,

$$\theta_G = \phi_G - \phi_0. \tag{7}$$

However, some pilot experiments indicated that θ_G detected by the above procedure turned oscillatory. This was not surprising because, although unintended, the robot propels with laterally undulating movements. However, this

Fig. 10 Notations in the robot experiment for the goal position

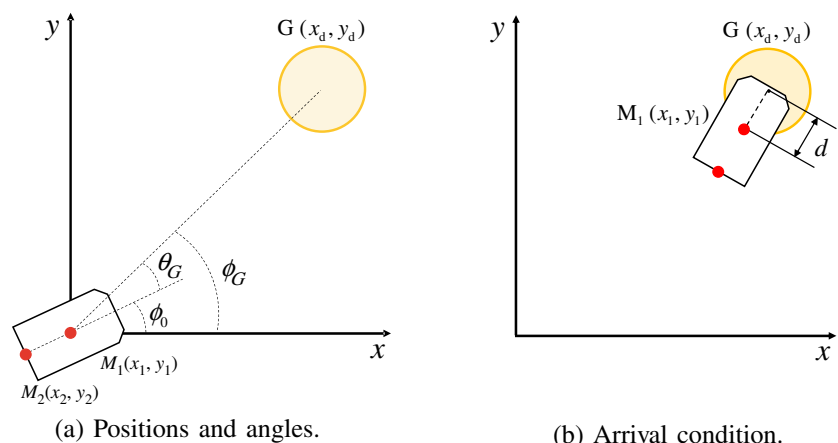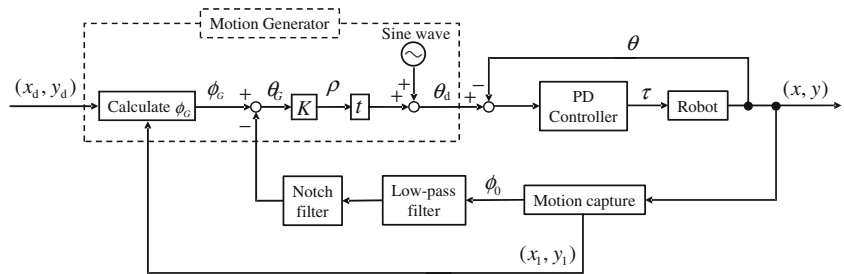(a) Positions and angles.

(b) Arrival condition.

Fig. 11 Block diagram

oscillation was affected by the adjustment of the offset rate of change and it destabilized the robot motion.

The undulating progression originated from periodic rotor rotations, implying that the frequency of oscillation in the detected θ_G is known in advance. In (3), f should generate the desired trajectory θ_{Rd}. Thus, after removing this frequency component from ϕ_0 using a notch filter and calculating θ_G, ρ was adjusted according to (4).

Finally, Figure 11 summarizes the controller as a block diagram.

4.4 Goal Reaching Experiments

4.4.1 Objects

We experimentally investigated whether the robot can reach a specified goal position based on the control method with the detection of the relative direction angle using a notch filter in the previous section. In addition, the effect of the magnitude of K was also examined.

4.4.2 Conditions

Experiments were conducted in the following conditions.

1. The goal position was set to G(240,100) when the start position was set to the origin $(0, 0)$ in the motion capture coordinate system.

2. $\alpha = 45°$ was selected for the range of the caster orientation. For θ_{Rd}, the parameters were set as $A = 55°$ and $f = 0.8$ Hz. Two initial phases $0°$ and $180°$ were tested.

3. The parameter K was changed from 100 to 220 in increments of 20.

4. The robot goes straight in the first period of the periodic rotor rotation.

5. The experiment was ended if the robot reached the area within $d = 25$ cm from the goal position.

(a) Original phase

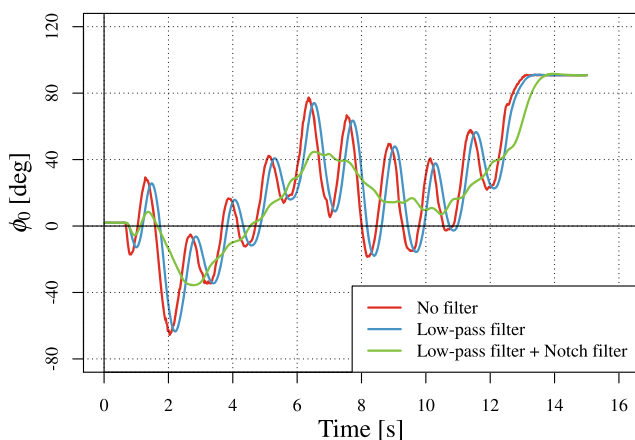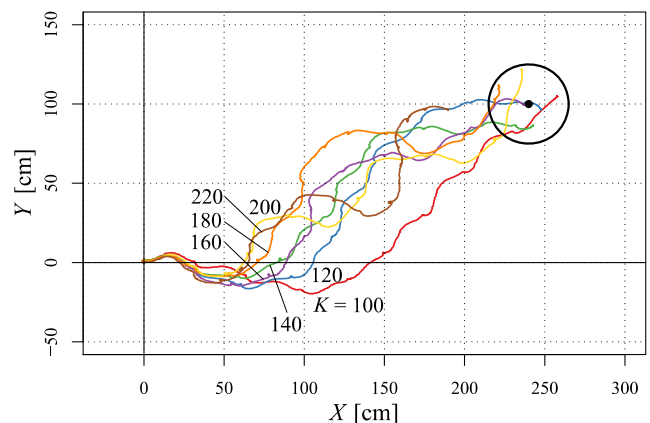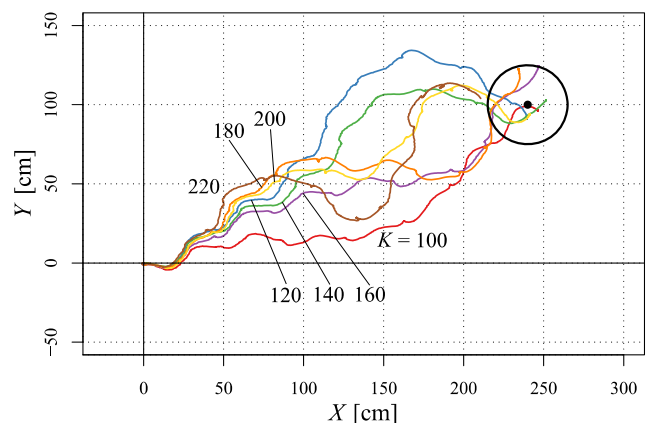**Fig. 12** Filtering result

(b) Anti-phase

Fig. 13 Experiments for traveling to the goal position

Table 1 Duration to the goal position

Original phase			Anti-phase		
K	Time [s]	Failure	K	Time [s]	Failure
100	11.0	1	100	9.3	0
120	10.6	0	120	9.6	1
140	11.1	0	140	9.7	0
160	11.2	0	160	9.7	0
180	12.5	0	180	10.8	0
200	12.3	1	200	12.3	0
220		3	220	13.2	1

6. The experiment was ended at 15 s even when the robot did not reach the goal.
7. Three experiments were conducted for each set of parameters.

A low-pass filter was introduced to remove noise in the encoder signal before applying a notch filter. Both filters were second-order filters with a sampling period of 20 ms and a damping factor of $1/\sqrt{2}$. The cut-off frequency of the low-pass filter was set to 1.5 Hz, and the notch frequency was set to 0.8 Hz. The feedback gains were set to $K_d = 0$ and $K_p = 1$, which is identical to that set in the previous section's experiments. If (3) was directly adopted for the generation of the desired rotor angle, the amount of offset change depended on the magnitude of t, implying that the offset changes differ, for example, in $t = 1$ and $t = 100$, even for the same ρ value. To avoid this, the change of the offset was implemented using the following integral:

$$\theta_{Rd} = A \sin(2\pi f t) + \theta_{\text{offset}} \tag{8}$$

$$\dot{\theta}_{\text{offset}} = K \times \theta_G. \tag{9}$$

4.4.3 Results

Figure 12 depicts the time course of the robot direction angle before and after the application of the filters. As expected, the oscillation originating from the undulating motion of the robot itself was removed.

Figure 13 illustrates the paths of the robot. The median path from each set of three experiments is depicted for each K. Furthermore, Table 1 summarizes the duration to the goal position and number of the failures. The duration to the goal position here is the average across the successful trials.

4.4.4 Remarks

When K is set to a large value, the robot tends to reach the goal position in a shorter duration because the offset rate of change is rapidly adjusted, and thus, the robot quickly faces the direction of the goal position. However, excessively large values of K, such as 220, enlarged the lateral undulation of the robot and resulted in the failure of the robot to reach the goal position within 15 s.

The robot reached the goal position in a shorter duration when the initial phase was set to 180°. This result is consistent with the data in Figure 7. When beginning from a non-moving state, the direction of motion slightly shifts toward the opposite orientation with respect to the first rotor swing owing to the gradual increase of the rotor swing amplitude in the transient state. In these experiments, the goal position existed ahead and to the right, and thus, the initial phase of 180° shifted the direction of movement to the right, which was advantageous.

(a) $\alpha = 35°$, $A = 55°$, f=0.7Hz   (b) $\alpha = 40°$, $A = 50°$, f=0.8Hz   (c) $\alpha = 45°$, $A = 55°$, f=0.9Hz
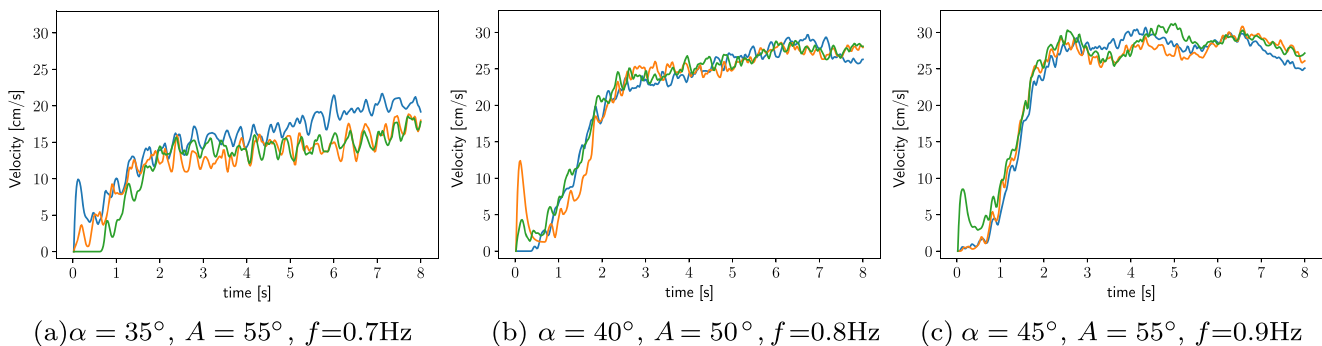
Fig. 14 Velocity profile during the experiments in the Section 3.4

(a) $\alpha = 35°$

(b) $\alpha = 40°$

(c) $\alpha = 45°$
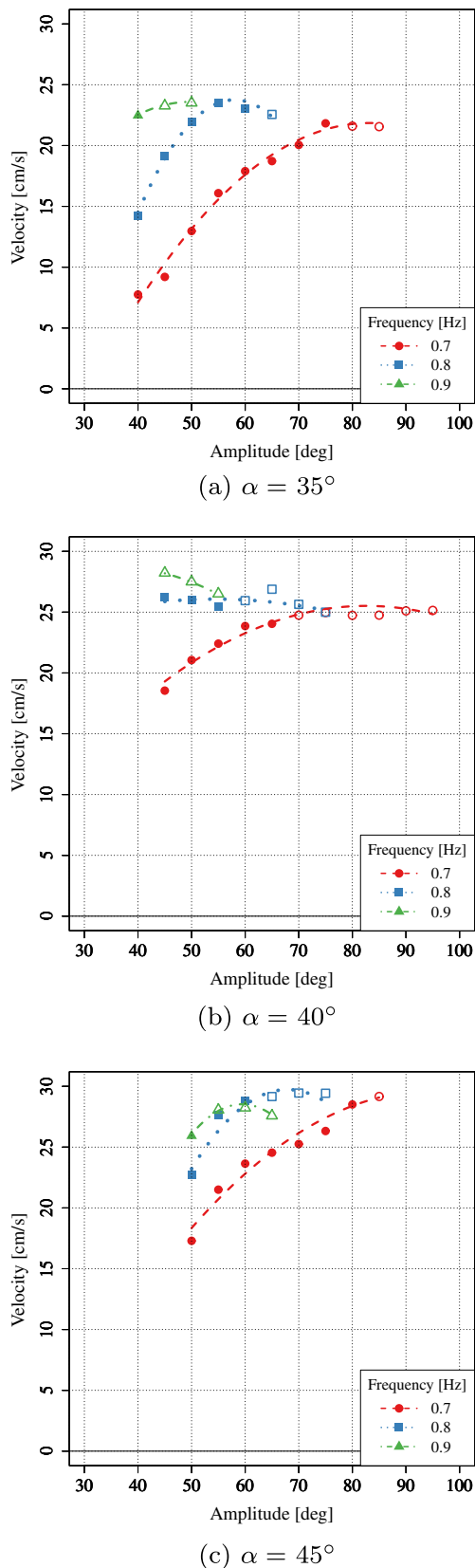
Fig. 15 Average velocity of the last 6-second motion in the straight

Although the robot was able to stop within 25 cm of the goal position, this distance should be reduced. However, the undulating movement of this robot and the lateral error due to this undulation affects movement accuracy of the robot. Further, the phase of the periodic rotor motion may be related to the accuracy at the moment of the goal. At this stage, it is difficult to reduce this effect; thus, the end point was designated as C5, where 25 cm is the entire length of the robot. The experiments in this study demonstrated that the accuracy in order of the robot size can be ensured at this time.

5 Discussion

5.1 Effect of Acceleration

In Section 3, the traveling distance was evaluated in terms of various parameters, such as the amplitude A or frequency f of the sinusoidal rotor motion, or the range of the wheel orientation α. Since the robot started from the still state, they are not exactly in a steady state. To investigate how the transient state is continuing, we calculated the velocity profile, where the velocity is computed using the difference in the positional data obtained from the motion capture system every 0.02 seconds. Three typical results after applying the notch (f and $2f$) and low-pass (15 Hz) filter are shown in Fig. 14.

All the data indicated that the acceleration period was approximately 2 seconds, indicating that the transient continues for 2 seconds. After that, some were slowly accelerated even more (Fig. 14a and b), and some were saturated (Fig. 14c). As shown in Fig. 14c, the final speed in the 8-second experiment tended to be larger than 25 cm/s, which provided a longer traveling distance, as shown in Fig. 6. Most of the final speed was distributed around 25cm/s for $\alpha = 40°$ or $45°$, though it differed from trial to trial even in the same conditions. The rigid preparation of the same experimental conditions was required to improve the reproducibility of the experimental results. As shown in Fig. 14a, the speed did not even reach 20 cm/s in some experiments for $\alpha = 35°$. We were able to estimate the speed of the robot from the distance shown in Fig. 6, but this result contained a 2-second transient effect or variance in the experiments. For this reason, we evaluated the average velocity excluding the first 2 seconds. The results were shown in Fig. 15. This provides the better evaluation of the robot's steady state.

5.2 Construction of Mathematical Model

To find a way to analyze the dynamics of this one-actuator mobile robot, a mathematical model was constructed and
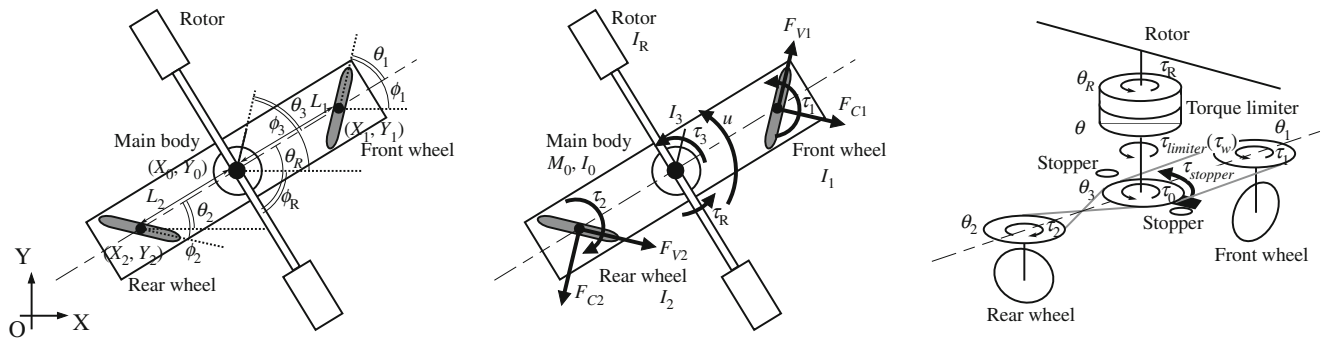
Fig. 16 A mathematical model of the robot

(a) Without friction ($\xi_R=0$)

(b) With friction ($\xi_R=1.0$)
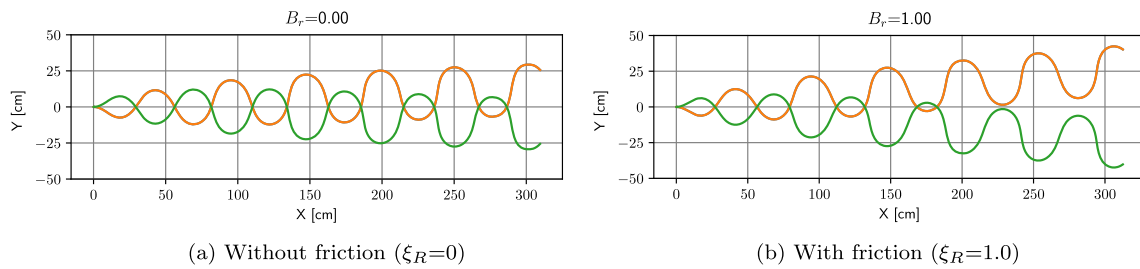
Fig. 17 Simulation of the straight movements

(a) $\alpha = 35°$

(b) $\alpha = 40°$

(c) $\alpha = 45°$
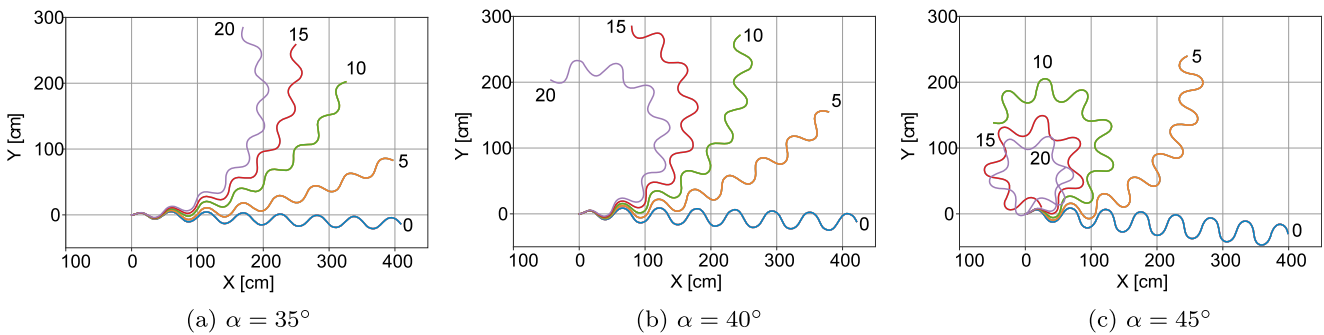
Fig. 18 Simulation of the curved movements

(a) $\rho = 0°/s$

(b) $\rho = 50°/s$
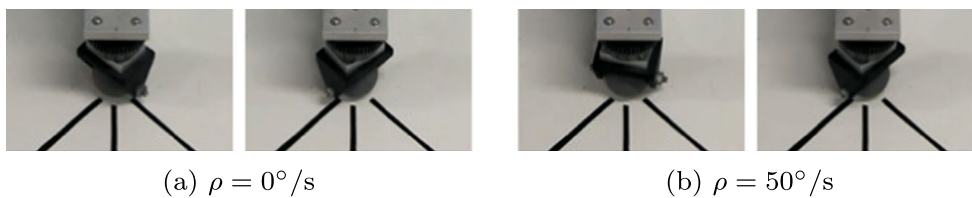
Fig. 19 Front wheel rotation in actual robot

Fig. 20 Simulation of the wheel orientation for $\alpha = 35°$

(a) $\rho = 30$

(b) $\rho = 50$
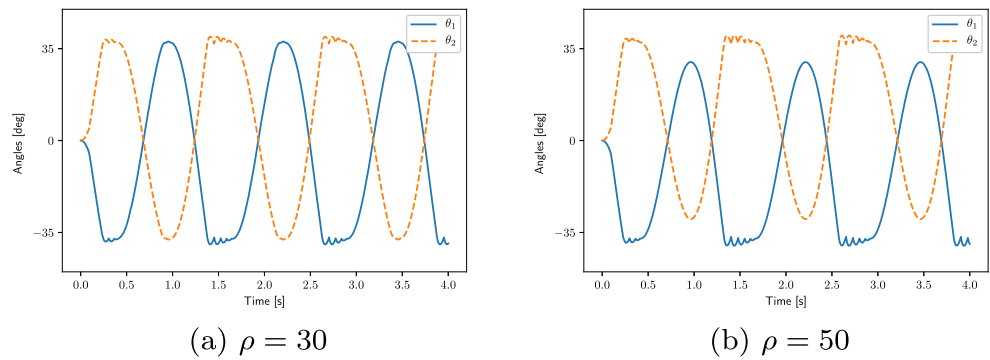
the difference between the dynamical behaviors of the actual robot experiments and the computer simulations were compared. The mathematical model is depicted in Fig. 16. The motion of this model was restricted to the horizontal plane. It consisted of the main body, front and rear wheels, the rotor, and the torque limiter. Two wheels were positioned symmetrically in the front-rear direction on the center line of the main body. The center of the mass of the main body, including mass of the wheels and the torque limiter, was assumed to be the center of the links of the main body. The rotation axis of the rotor was also set at the center of mass of the main body. The robot was assumed to maintain its lateral balance, and the collision between the bar and the stoppers were represented using a spring and a dumper with the high elasticity and viscosity.

The torque limiter disconnects the torque transmission if a large torque is exerted. Such a function is modeled here as the linear element with the saturation:

$$\tau_{limier}(\tau) = \begin{cases} \tau_{min} & (\tau < \tau_{min}) \\ \tau & (\tau_{min} \leq \tau \leq \tau_{max}) \\ \tau_{max} & (\tau > \tau_{max}) \end{cases} \quad (10)$$

where, $\tau_{limiter}$ and τ are the output and input of the torque limiter, respectively, and $\tau_{min} < 0$ and $\tau_{max} > 0$ represent the limits of torque values in the negative or positive rotating direction, respectively. This indicates that a torque less than τ_{min} and larger than τ_{max} is never transmitted via the torque limiter.

The motion equation of the model is described in the appendices with its derivation processes.

First of all, we examined whether this model could make progress by zeroing the friction coefficient of the rotor rotation. The model ran forward successfully, as shown in Fig. 17, where the same control method was employed with $A = 50°$, $f = 0.8$ Hz, $\alpha = 45°$, $K_d = 0.05$, and $K_p = 1$. This result was different from the experimental result in Fig. 7, as in that the orbit did not deviate from the initial

direction. However, adding the effect of friction around the motor, $\xi_R = 0.5$, deviated the motion to the side opposite to the initial rotor rotation, as observed in the simulation. This made it possible to conclude that one of the reasons for the orbit deviation in Fig. 7 originated from the friction of the rotor rotation.

We then tried simulating curved movement, as shown in Fig. 8 using this mathematical model, with the results shown in Fig. 18. The curved movements were qualitatively presented, especially in that the curvature of the orbit increased as ρ, increased, which resulted in the offset of the sinusoidal input. The model ran longer and turned shaper compared to the real robot behavior. However, the straight movements at the small ρ in $\alpha = 35°$ and $40°$, respectively, and did not appear in our simulations.

5.3 Actual Wheel Rotation in Curved Motion

The Section 3.5.3 predicted that the reason for the curved motion of the robot was the difference in the rotation angle between the left and right orientation. If true, it will be possible to observe the phenomena even in the off-ground robot motions. Figure 19 shows photos at the moment when the front wheel angle reaches the limit on both sides, respectively, for $\alpha = 35°$. The wheel angle reached the right limit marked on the floor at a small $\rho = 0$, whereas it returned before reaching the left limit. These photos demonstrate that the unequal deviation in wheel rotation was definitely occurring.

We then turned our attention to determining whether the same phenomenon was occurring in the simulation. Figure 20 shows the time-course of the wheel orientation for $\alpha = 35°$. As shown in Fig. 19, the wheel orientation reached the limit of motion (for $\alpha = 35°$ at $\rho = 30$, while it does not at $\rho = 50$. The latter will surely contribute to the curved movement, but the former will also be able to produce the curved motion. This is simply our first idea mentioned in

the Section 3.5.3. The reasons why the actual robot not only differs from our first idea but also the simulations are still unanswered questions for us. To simulate this non-curved behavior, the rotor moment with respect to the main body should balance in the CW and CCW direction. From this perspective, it is necessary to model the dynamics and improve the mathematical model to describe the behavior in a realistic manner.

6 Conclusion

To develop a novel maneuvering mechanism, we designed, constructed, and conducted experiments on a robot with passive wheels, inspired by the two-wheeled skateboard. The notable characteristic of this design is that the robot is driven using a single motor. In the robot design, the orientations of the front and rear casters are coupled, and then, a rotor driven by the sole motor is connected to the front and rear casters via a torque limiter. The range of motion of the caster orientation is restricted by stoppers, which mechanically control the orientation of the casters. However, these stoppers do not restrict rotor rotation because the torque limiter disconnects the coupling between the caster orientation and rotor rotation when the stopper is working.

Using the robot thus constructed, we conducted several experiments, which demonstrated that sinusoidal movement from the rotor produced straight propulsion, and the offset increment or decrement of the sinusoidal drive caused the robot to curve to the left and right. In addition, a method to move the robot to a specified goal position using feedback of the current position and direction of the robot was proposed and tested. Although the goal position must be far enough from the start position, the robot could reach the goal position using straight progression after it changed its orientation such that the goal position was nearly directly ahead.

Finally, the mathematical model of this robot was constructed, and it qualitatively described the straight and curved movements, but did not explain why the robot moved straight for a small increase in the offset in sinusoidal rotor rotation for the small rotation range of the wheels. It may be necessary to reconsider the model of the torque limiter or introduce the effect of the side support in the mathematical model.

Future work would include controlling the robot to reach the goal position from any designated direction.

Appendix

A1 Motion Equation

The position and the orientation of the man body, the front and the rear wheel are denoted by (X_0, Y_0, ϕ_0), (X_1, Y_1, ϕ_1) and (X_2, Y_2, ϕ_2), respectively. The positional relationship among them is represented as follows:

$$X_1 = X_0 + L_1 \cos \phi_0 \tag{11}$$

$$Y_1 = Y_0 + L_1 \sin \phi_0 \tag{12}$$

$$X_2 = X_0 - L_2 \cos \phi_0 \tag{13}$$

$$Y_2 = Y_0 - L_2 \sin \phi_0 \tag{14}$$

Here, L_1 and L_2 are the distance from the center of the main body to each wheel. The velocity of the front and rear wheel normal to the wheel axis, V_1 and V_2, are given as follows:

$$V_i = \dot{X}_i \cos \phi + \dot{Y}_i \sin \phi \tag{15}$$

while the constraints that keep the wheels from slipping to each wheel axis direction are written as follows:

$$V_i^{\perp} \equiv \dot{X}_i \sin \phi - \dot{Y}_i \cos \phi \tag{16}$$

where, $i = 1, 2$ distinguishes the front and rear wheels.

The rotor, the torque limiter and the wheels move together with the main body. The main body dynamics is obtained as the following motion equation:

$$M\ddot{Q} = J_C^T F_C + J_V^T F_V + J_U^T u + F_f \tag{17}$$

Here, $Q = \begin{bmatrix} X_0 & Y_0 & \phi_0 \end{bmatrix}^T$ is the state vector of the main body, M is the inertial matrix whose components are given by the total mass of the main body including the rotor and wheels M_0, and the moment of inertial of the main body I_0 (without rotor),

$$M = \begin{bmatrix} M_0 & 0 & 0 \\ 0 & M_0 & 0 \\ 0 & 0 & I_0 \end{bmatrix} \tag{18}$$

J_C and J_V are the Jacobian matrices

$$J_C = \begin{bmatrix} \sin \phi_1 & -\cos \phi_1 & -L_1 \cos(\phi_1 - \phi_0) \\ \sin \phi_2 & -\cos \phi_2 & L_2 \cos(\phi_2 - \phi_0) \end{bmatrix} \tag{19}$$

$$J_V = \begin{bmatrix} \cos \phi_1 & \sin \phi_1 & L_1 \sin(\phi_1 - \phi_0) \\ \cos \phi_2 & \sin \phi_2 & -L_2 \sin(\phi_2 - \phi_0) \end{bmatrix} \tag{20}$$

that relates $\dot{Q}$ to

$$V^{\perp} = [\, V_1^{\perp} \;\; V_2^{\perp} \,]^T \tag{21}$$

$$V = [\, V_1 \;\; V_2 \,]^T \tag{22}$$

respectively, and $F_C = \begin{bmatrix} F_{C1} & F_{C2} \end{bmatrix}^T$ is the constraint force that prevents each wheel from slipping to the wheel axis

direction, $F_V = \begin{bmatrix} F_{V1} & F_{V2} \end{bmatrix}^T$ is the resistance force against the wheel rotation or progression such as the friction. F_f is the friction force, given by the following equation:

$$F_f = [\,0\ 0\ \xi_R \dot{\theta}_R\,]^T \tag{23}$$

See the Section I for θ_R and ξ_R. J_U becomes as follws:

$$J_U = \begin{bmatrix} 0 & 0 & 1 \end{bmatrix} \tag{24}$$

And, u is control input, i.e., the counter force against the rotor rotation $u = -\tau$.

A2 Velocity Constraints

The wheel is assumed not to slip in its wheel-axis direction. This condition is equivalent to $V^\perp == 0$, which is written using the derivative of (11)–(14) as follows:

$$J_C \dot{Q} = 0 \tag{25}$$

A3 Resistance Force

As the resistance force applied to the wheel motion, the viscous friction is considered. Then, F_V is represented as follows:

$$F_V = -BV = -BJ_V\dot{Q} \tag{26}$$

where, B is the viscous matrix:

$$B = \begin{bmatrix} b_1 & 0 \\ 0 & b_2 \end{bmatrix} \tag{27}$$

b_1 and b_2 are the viscous coefficients corresponding to each wheel.

A4 Stopper

The collision and contact between the bar and stoppers are modeled as the spring and the dumper, which generates the reaction torque $\tau_{stopper}$ around the wheel rotation.

$$\tau_{stopper}(\theta) = \begin{cases} -b_s\dot{\theta} + k_s(\theta_+ - \theta) & (\theta > \theta_+) \\ 0 & (\theta_- < \theta_M < \theta_+) \\ -b_s\dot{\theta} + k_s(\theta_- - \theta) & (\theta < \theta_-) \end{cases} \tag{28}$$

A5 Coupling Dynamics of Wheel Orientations

Put the orientation angle of the front and the rear wheel relative to the main body as $\theta_1 = \phi_1 - \phi_0$ and $\theta_2 = \phi_2 - \phi_0$, respectively, and let the torque limiter angle relative to the main body θ_3. Their dynamics are given as follows:

$$I_1\ddot{\theta}_1 = -\xi_1\dot{\theta}_1 + \tau_1 \tag{29}$$

$$I_2\ddot{\theta}_2 = -\xi_2\dot{\theta}_2 + \tau_2 \tag{30}$$

$$I_3\ddot{\theta}_3 = -\xi_3\dot{\theta}_3 + \tau_3 \tag{31}$$

Here, ξ_1, ξ_2, ξ_3 are the viscous coefficients of the rotation around the front wheel, the rear wheel, and the rotor, and τ_1, τ_2 and τ_3 are the torque around them, respectively. The coupling of the wheel orientation imposes the following constraints:

$$\theta_1 = \gamma_1\theta, \theta_2 = \gamma_2\theta, \theta_3 = \theta \tag{32}$$

$$\tau_1 + \tau_2 + \tau_3 = \tau_w \tag{33}$$

Besides, the stopper limits the range of the rotation, and the torque generated by the motor is transmitted via the torque limiter. Considering all of them, the rotation of the wheel orientation is solely represented by the following dynamics of θ because of the coupling (33)

$$(|\gamma_1|I_1 + |\gamma_2|I_2 + I_3)\ddot{\theta} = -\,(|\gamma_1|\xi_1 + |\gamma_2|\xi_2 + \xi_3)\dot{\theta} \\ + \tau_{stopper} + \tau_{limiter}(\tau_w) \tag{34}$$

A6 Rotor

The motion of the rotor is simply modeled as the rotation of the rigid bar.

$$I_R\ddot{\theta}_R = -\xi_R\dot{\theta}_R + \tau_R \tag{35}$$

Here θ_R is the rotor angle relative to the main body, I_R is the moment of inertia of the rotor, ξ_R is the friction coefficient of the rotor rotation, and τ_R denotes the driving moment.

A7 Actual Computation

The degrees of freedom of this system becomes five, i.e., X_0, Y_0, ϕ_0, θ and θ_R. The state of the main body is represented by X_0, Y_0 and ϕ_0, whose dynamics are given by (17) with the velocity constraint (16), and is driven as the torque $-\tau$.

Then, its reaction force τ rotates the rotor as well as the wheel orientation. Namely,

$$\tau = \tau_R + \tau_w \tag{36}$$

However, the dynamics of the rotor and the wheel orientation varies depending on whether the torque limiter is on or off.

If the torque limiter is off, the wheel orientation changes with the rotor rotation and the coupling relation

$$\dot{\theta} = \gamma\dot{\theta}_R \tag{37}$$

holds. Accordingly, (34) and (35) should be solved under this condition which allows us to get $\ddot{\theta}(= \ddot{\theta}_R)$. Now, we can obtain the value of the $\tau_{limiter}(\tau_w)$ from this $\ddot{\theta}$, using (34). Here,

a. The case $\tau_{min} \leq \tau_{limiter}(\tau_w) \leq \tau_{max}$:
   The torque limiter is actually off. Thus, we should continue the calculation without any modification.

b. The case $\tau_{limiter}(\tau_w) < \tau_{min}$:
   The torque limiter should disconnect the torque transmission. Thus, put $\tau_w = \tau_{min}$ and calculate (34) and (35) again removing condition (37).

c. The case $\tau_{limiter}(\tau_w) > \tau_{max}$:
   The torque limiter should disconnect the torque transmission. Thus, put $\tau_w = \tau_{max}$ and calculate (34) and (35) again removing condition (37).

Finally, we should mention the calculation for the moment at which the torque limiter switches from on to off. In this moment, the two different rotations, $\dot{\theta}$ and $\dot{\theta}_R$, are coupled and starts to rotate with the same speed $\dot{\theta}_{new}$. This $\dot{\theta}_{new}$ is calculated considering the conservation of the angular moment:

$$(|\gamma_1|I_1 + |\gamma_2|I_2 + I_3)\dot{\theta} + I_R\dot{\theta}_R = (|\gamma_1|I_1 + |\gamma_2|I_2 + I_3 + I_R)\dot{\theta}_{new} \tag{38}$$

Namely, the rotation speed jumps at this moment.

A8 Default Parameters

The Rung-Kutta method with 0.0001 second step size was utilized for the simulations. The followings are default parameter values in the simulations when any other descriptions are now shown: $M = 4$, $I_0 = 0.08$, $I_1 = I_2 = 0.002$, $I_3 = 0.001$, $I_R = 0.05$, $L_1 = L_2 = 0.1$, $\gamma_1 = 1$, $\gamma_2 = -1$, $\gamma = 1$, $\xi_0 = 0.01$, $\xi_1 = \xi_2 = \xi = 0$, $\xi_R = 0.1$, $b_1 = b_2 = -3$, $b_s = 0.2$, $k_s = 5$, $\theta_{L+} = +\alpha$, $\theta_{L-} = -\alpha$. $\tau_{min} = -0.1$, $\tau_{max} = 0.1$,

References

1. Kajita, S., Kanehiro, F., Kaneko, K., Yokoi, K., Hirukawa, H.: The 3d linear inverted pendulum mode: A simple modeling for a biped walking pattern generation. In: Proceedings. 2001 IEEE/RSJ International Conference on Intelligent Robots and Systems, 2001, vol. 1, pp. 239–246 IEEE (2001)
2. Goswami, A., Thuilot, B., Espiau, B.: A study of the passive gait of a compass-like biped robot Symmetry and chaos. Int. J. Robot. Res. 17(12), 1282–1301 (1998)
3. Hirose, S.: Three basic types of locomotion in mobile robots. In: Fifth International Conference on Advanced Robotics 'Robots in Unstructured Environments', pp. 12–17. IEEE (1991)
4. Hirose, S., Yamada, H.: Snake-like robots [tutorial]. IEEE Robot. Autom. Mag. 16(1), 88–98 (2009)
5. Takemori, T., Tanaka, M., Matsuno, F.: Gait design for a snake robot by connecting curve segments and experimental demonstration. IEEE Transactions on Robotics (2018)
6. Ariizumi, R., Tanaka, M., Matsuno, F.: Analysis and heading control of continuum planar snake robot based on kinematics and a general solution thereof. Adv. Robot. 30(5), 301–314 (2016)
7. Krishnaprasad, P.S., Tsakiris, D.P.: Oscillations, Se (2)-snakes and motion control: A study of the roller racer. Dynamical Systems: An International Journal 16(4), 347–397 (2001)
8. Mori, H., Nagamine, T., Ichuo, T., Sato, Y.: Effects of friction on driving mechanism using swing motion. Transactions of the JSME (in Japanese) 81(832), 15–00330 (2015)
9. Iannitti, S., Lynch, K.M.: Minimum control-switch motions for the snakeboard: A case study in kinematically controllable underactuated systems. IEEE Trans. Robot. 20(6), 994–1006 (2004)
10. Ostrowski, J.: Steering for a class of dynamic nonholonomic systems. IEEE Trans. Autom. Control 45(8), 1492–1498 (2000)
11. Narikiyo, T.: Control of underactuated mechanical systems via passive velocity field control: Application to snakeboard and 3D rigid body. Nonlinear Anal. 71, e2358–e2365 (2009)
12. Shammas, E., De Oliveira, M.: Motion planning for the snakeboard. Int. J. Robot. Res. 31(7), 872–885 (2012)
13. Derammelaere, S., Copot, C., Haemers, M., Verbelen, F., Vervisch, B., Ionescu, C., Stockman, K.: Realtime locomotion control of a snakeboard robot based on a novel model, enabling better physical insights. European Journal of Control (2018)
14. Salman, H., Dear, T., Babikian, S., Shammas, E., Choset, H.: A Physical parameter-based skidding model for the snakeboard. In: 2016 IEEE 55Th Conference on Decision and Control (CDC), pp. 7555–7560 (2016)
15. Wang, T., Su, B., Kuang, S., Wang, J.: On kinematic mechanism of a two-wheel skateboard: The essboard. J. Mech. Robot. 5(3), 034503 (2013)
16. Su, B., Wang, T., Wu, R., Wang, J.: Infimum of path length of nonholonomic vehicle with finitely bounded curvature radius. J. Intell. Robot. Syst. 79(2), 197–210 (2015)
17. Kinugasa, K., Ishikawa, M., Sugimoto, Y., Osuka, K.: Modeling and control of casterboard robot. IFAC Proceedings Volumes 46(23), 785–790 (2013)
18. Ito, S., Sugiura, S., Masuda, Y., Kiely, S., Yabuki, J., Morita, R.: A mechanism of single actuator snakeboard robot and its curving motion generation. In: 2018 IEEE International Conference on Robotics and Biomimetics (IEEE ROBIO 2018), pp. 1232–1237 (2018)
19. Bullo, F., Lewis, A.D.: Kinematic controllability and motion planning for the snakeboard. IEEE Trans. Robot. Autom. 19(3), 494–498 (2003)

Satoshi Ito received the B. E. and M. E. degrees, respectively in 1991 and 1993 from Nagoya University, Japan. He was with Bio-Mimetic Control Research Center, RIKEN, Japan, as a technical staff from 1994 to 1997 and a Frontier Researcher from 1997 to 1999. In 1999, he received the Dr. Eng. degree from Nagoya University. He was a research associate at the Faculty of Engineering, Gifu University, Japan, in 1999, and was an associate professor in 2004. He has been a professor at Gifu University since 2015.

Shoya Sugiura received the B.S. degree in engineering from Gifu University, Japan, in 2018. He is currently a student of graduate school of Natural Science and Technology, Gifu University.

Yuya Masuda received the B.S. degree in engineering from Gifu University, Japan, in 2017. He is currently with Mitsubishi Hitachi Home Elevator Corporation.

Shumpei Nohara received the B.S. degree in engineering from Gifu University, Japan, in 2017. He is currently with Hitachi Zosen Corporation.

Ryosuke Morita received the B.S. degree in engineering, the M.S. and Ph.D. degree in informatics from Kyoto University, Kyoto, Japan in 2008, 2010, and 2013 respectively. From 2013 to 2014, he was a Specially Appointed Researcher in Graduate School of Information Science and Technology, Osaka University, Suita Japan. From 2014 to 2015, he was an Assistant Professor of the College of Science and Engineering, Aoyama Gakuin University, Sagamihara, Japan. He is currently an Assistant Professor of the Faculty of Engineering, Gifu University, Gifu, Japan.